Enhanced Sensitivity in Photovoltaic 2D MoS₂/Te Heterojunction VOC Sensors

Mohammad Reza Mohammadzadeh, Amirhossein Hasani, Tanveer Hussain, Hamidreza Ghanbari, Mirette Fawzy, Amin Abnavi, Ribwar Ahmadi, Fahmid Kabir, Thushani De Silva, R. K. N. D. Rajapakse, and Michael M. Adachi*

Volatile organic compound (VOC) sensors have a broad range of applications including healthcare monitoring, product quality control, and air quality management. However, many such applications are demanding, requiring sensors with high sensitivity and selectivity. 2D materials are extensively used in many VOC sensing devices due to their large surface-to-volume ratio and fascinating electronic properties. These properties, along with their exceptional flexibility, low power consumption, room-temperature operation, chemical functionalization potential, and defect engineering capabilities, make 2D materials ideal for high-performance VOC sensing. Here, a 2D MoS₂/Te heterojunction is reported that significantly improves the VOC detection compared to MoS₂ and Te sensors on their own. Density functional theory (DFT) analysis shows that the MoS₂/Te heterojunction significantly enhances the adsorption energy and therefore sensing sensitivity of the sensor. The sensor response, which denotes the percentage change in the sensor's conductance upon VOC exposure, is further enhanced under photo-illumination and zero-bias conditions to values up to ≈7000% when exposed to butanone. The MoS₂/Te heterojunction is therefore a promising device architecture for portable and wearable sensing applications.

1. Introduction

Volatile organic compounds (VOCs) are organic molecules primarily composed of carbon and hydrogen atoms that can readily evaporate at room temperature and atmospheric pressure.[1] VOCs can be emitted from both biological and industrial sources that can affect indoor and outdoor air quality.[2] Long-term exposure to VOCs can be harmful to human's health, resulting in various health problems and diseases such as cancer, skin irritation, impairment of the nervous system, and lung damage.[3,4] By monitoring VOC levels, proactive measures to improve indoor air quality can be taken, ensuring healthier living and working conditions.

Human metabolic pathological processes also release VOC molecules to the environment. These VOCs can be used as biomarkers associated with our clinical and nutritional status to diagnose and monitor the onset of diseases using noninvasive methods.[5] Research has shown a connection between certain VOCs such as 2-butanone and acetone to various health conditions or diseases including lung cancer and diabetes.[6,7] An elevated concentration of the VOCs in patient samples such as exhaled breath or sebum can therefore be used to non-invasively screen patients for diseases, potentially leading to better preventive strategies and early treatments.[8] Considering the adverse effects of VOCs on air quality, human health, and their potential association with diseases, the development of highly sensitive and selective VOC sensors has potential to improve workplace safety and healthcare.

M. R. Mohammadzadeh, A. Hasani, H. Ghanbari, A. Abnavi, R. Ahmadi, F. Kabir, T. De Silva, R. K. N. D. Rajapakse, M. M. Adachi
School of Engineering Science
Simon Fraser University
Burnaby, British Columbia V5A 1S6, Canada
E-mail: mmadachi@sfu.ca

T. Hussain
School of Science and Technology
University of New England
Armidale, New South Wales 2351, Australia

M. Fawzy
Department of Physics
Simon Fraser University
Burnaby, British Columbia V5A 1S6, Canada

A. Hasani
Department of Physics and MonArk NSF Quantum Foundry
Montana State University
Bozeman, MT 59717, USA

R. K. N. D. Rajapakse
Faculty of Engineering
Sri Lanka Institute of Information Technology
New Kandy Road, Malabe 10115, Sri Lanka

There are a number of methods for detecting VOC molecules including gas chromatography-mass spectrometry (GC-MS) and infrared spectrometry. However, these methods are expensive and have limited portability. Chemiresistive sensors prepared by scalable microfabrication techniques are miniature, portable, and have low power consumption, making them suitable for next-generation applications such as wearable internet of things (IoT) devices.[9,10]

One class of materials that have inspired many research areas over the past decade in electronics, optoelectronics, energy storage, catalysis, and chemical sensing is 2D materials.[11–13] Benefiting from a crystalline ultrathin structure, high carrier mobility, and surface-sensitive tunable electronic band structure, 2D materials can offer exceptional sensitivity and selectivity in chemical sensing applications, which is particularly crucial for diagnostic applications.[14,15] Moreover, they can operate at room temperature, making them a low-power consumption alternative to conventional sensing materials such as metal oxides, which typically operate at elevated temperatures. The 2D materials family encompasses a diverse range of materials including graphene, transition metal dichalcogenides (TMDs), hexagonal boron nitride (h-BN), transition metal carbides/nitrides (MXenes), and black phosphorus (BP).[16] As one of the most outstanding classes of the 2D material family, TMDs including MoS_2, WS_2, $MoSe_2$, and WSe_2 have shown exceptional promise in gas sensing field. Among TMDs, molybdenum disulfide (MoS_2) is the most extensively studied TMDs in gas sensing application.[17] Besides MoS_2's unique thickness-dependent electrical/chemical properties and high adsorption coefficient, its remarkable mechanical properties of enduring high strains up to 11% and its potential to be integrated into conventional integrated circuits (ICs) make it suitable for flexible electronics devices and advanced wearable sensors.[18]

2D tellurium (Te) is the new member of the monoelemental 2D materials family that has shown promising potential in next-generation electronic and optoelectronic applications owing to its unique quasi-1D atomic chain structure, high carrier mobility (up to $1000 \, cm^2V^{-1}s^{-1}$ at room temperature), strong light-matter interaction, and better environmental stability.[19] Moreover, the surface of 2D Te is free of dangling bonds, which is ideal for making heterostructures of different 2D materials that have diverse energy band alignments.[20] Although there are booming research endeavors on 2D Te-based field effect transistors (FETs) and optoelectronic devices, the research on 2D Te in gas sensing applications is still in its early stage.
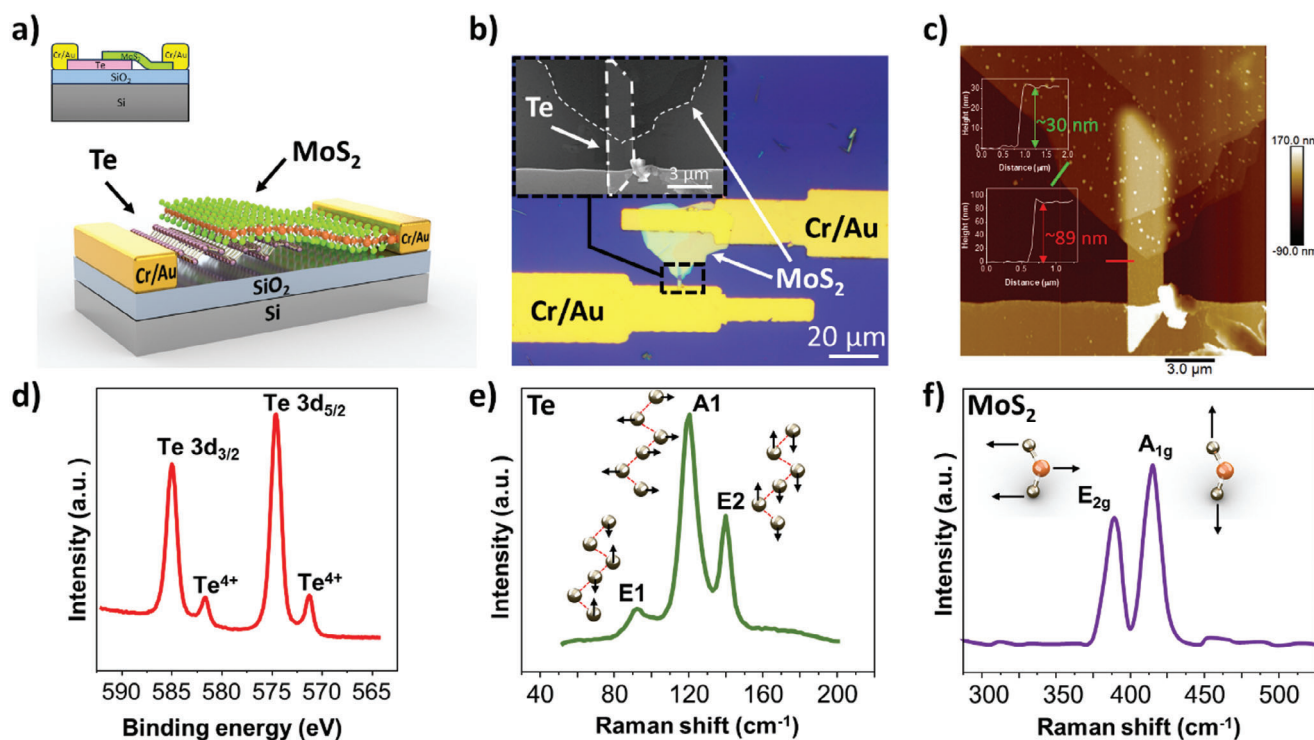
Heterojunctions between appropriate 2D materials have been investigated for the detection of inorganic gases such as NO_2 or NH_3.[21–26] For example, Niu et al. achieved the detection of very low concentrations of NO_2 in parts-per-billion (ppb)-level using a photovoltaic sensor based on a MoS_2/GaSe heterojunction.[27] However, to the best of our knowledge, sensitivity enhancement using a heterojunction device architecture based on 2D materials and its influence on sensor adsorption energy have yet to be reported for the detection of VOCs.

In this work, we demonstrate a photovoltaic VOC sensor based on a MoS_2 (n-type)/Te (p-type) heterojunction. The mechanically exfoliated 2D MoS_2 crystals were transferred on the hydrothermally synthesized 2D Te nanoflakes to create a type I p-n junction at the interface. Alternatively, a bottom-up approach, such

as chemical vapor deposition (CVD), physical vapor deposition (PVD), ultra-high vacuum (UHV)-assisted synthesis, atomic layer deposition (ALD), and E-beam evaporation, can be employed to prepare the heterostructure.[28] In these bottom-up approaches, the layered structure of MoS_2 and Te can be deposited layer by layer on the substrate with an atomic precision by controlling several parameters including precursor concentration, carrier gas, temperature, and distance from the substrate.[29] While bottom-up approaches ensure consistency in the number of layers and the dimensions of the heterostructure across different devices, top-down approaches such as mechanical, chemical, or liquid exfoliation can produce high-quality materials at low cost for proof-of-concept studies. The flakes obtained through these approaches generally maintain their structural integrity and are less prone to defects although some variation in properties between exfoliated flakes may occur.[29] The efficient carrier transport modulation between the two materials and stronger adsorption of VOCs on the heterojunction, supported by density functional theory (DFT) simulations, result in excellent sensing performance toward six different VOCs. The MoS_2/Te device exhibited its best VOC sensing sensitivity under illumination at zero bias voltage, demonstrating a response of up to ≈7000% (i.e., the sensor's initial conductance increased by 7000%) when exposed to 100 ppm butanone, the highest reported in the literature for zero-bias room-temperature VOC sensors.

2. Results and Discussion

The van der Waals MoS_2/Te heterojunction was fabricated by stacking mechanically-exfoliated MoS_2 nanoflakes on hydrothermally synthesized 2D Te nanosheets as illustrated in **Figure 1a**. The first Cr/Au electrode was deposited on top of the multilayer Te flake. The multilayer MoS_2 flake was then transferred onto the substrate, overlapping with the Te nanoflake, and electrically contacted with a second deposited Cr/Au electrode. Figure 1b illustrates the optical microscopic image of the fabricated heterojunction device. A scanning electron microscopy (SEM) image shown in the inset of Figure 1b provides a magnified view of the overlapping region between the MoS_2 nanosheet and Te flake. Atomic force microscopy (AFM) measurements determined a MoS_2 thickness of ≈30 nm and Te thickness of ≈89 nm (Figure 1c). The chemical composition and surface chemistry of the synthesized Te samples were investigated using X-ray photoelectron spectroscopy (XPS). The XPS spectra shown in Figure 1d, have two strong peaks at 584.8 and 574.4 eV corresponding to Te $3d_{5/2}$ and Te $3d_{3/2}$, respectively, which are indicative of pure and clean Te growth without any residual metal atoms. The slight oxidation of Te on the surface, however, resulted in the two weak peaks at 571.1 and 581.5 eV, which correspond to the binding energy of the Te^{4+} cations to the oxygen atoms.[30] The Raman spectra of 2D Te and MoS_2 flakes are shown in Figure 1e,f, respectively. The two peaks of degenerate E mode at 91 and 143 cm^{-1} and a dominant peak at 121 cm^{-1} related to the A_1 mode are the fingerprint peaks of multilayer Te.[31] The two prominent peaks observed in the Raman spectrum of the MoS_2 flake correspond to the in-plane mode (E_{2g}) at 384 cm^{-1} and the out-of-plane mode (A_{1g}) at 408 cm^{-1}, confirming its 2H semiconducting phase.[32]

ADVANCED
SCIENCE NEWS
www.advancedsciencenews.com

NANO · MICRO
small
www.small-journal.com

Figure 1. MoS_2/Te VOC sensor and characterization of the device. a) 3D schematic illustration and cross-sectional view (inset) of heterojunction device; b) top-view optical microscopy image of the fabricated MoS_2/Te sensor; SEM image of the top view of the MoS_2/Te heterojunction is shown in the inset; c) AFM height map and height profile (inset) of the MoS_2 and Te flakes; d) XPS spectra of the-as synthesized Te crystal; Raman spectra of e) the Te and f) MoS_2 crystals.

## 2.1. VOC Sensing Properties Under Dark Conditions

The VOC sensing characteristics of the heterojunction were first measured at 2 V reverse bias voltage under dark conditions as shown schematically in **Figure 2a**. The time-resolved sensor response of the device toward ethanol is shown in Figure 2b, where the sensor response $(\Delta G/G_0)$ is defined as a ratio between the change in conductance (ΔG) due to VOC exposure and its original conductance before VOC exposure (G_0). As shown in Figure 2b, the response toward ethanol monotonically increases from 11 to 26 as the VOC concentration rises from 50 to 300 parts per million (ppm). The device shows a high response of 1500% (i.e., $\Delta G/G_0 = 15$) when exposed to 100 ppm ethanol, which is higher than other 2D materials-based VOC sensors reported in the literature.[33] The time-resolved device responses to other VOCs, including acetone, 2-propanol (IPA), 1-propanol, and butanone, at different concentrations are shown in Figure S1 (Supporting Information).

The response time, defined as the duration of time from the introduction of the VOC to when the response reaches 90% of its peak value was measured to be 80 s when exposed to 50 ppm of ethanol under dark conditions (Figure 2c). Similarly, the recovery time, or the duration of time required for the device to reach 10% of its maximum response value after the VOC was removed was 26 s. The response and recovery times of VOC sensors depend on adsorption/desorption kinetics, the physical and chemical properties of VOCs, and experimental conditions. Adsorption, the primary mechanism affecting sensor response,

includes physisorption and chemisorption, each involving different binding forces and kinetics.[34,9] Physisorption, involving van der Waals forces and hydrogen bonding, occurs rapidly but weakly, while chemisorption, forming valence bonds, is stronger and less reversible, impacting sensor recovery times.[35,36] Factors like operating temperature and VOC concentration further influence these kinetics, with temperature increases accelerating both processes.[10,37,38] Additionally, the physical and chemical properties of VOCs, such as molecular weight and diffusion coefficients, significantly affect sensor response times.[39–41] Experimental conditions, including the design of the measurement setup and whether a dynamic or static method is used, also play crucial roles in determining response times.

The selectivity characteristics of the heterojunction were investigated by comparing the sensor response toward 100 ppm of 1-propanol, butanone, ethanol, 2-propanol, and acetone. As shown in Figure 2d, the device exposed to six different VOCs under dark condition exhibited its highest response to polar-protic molecules such as ethanol and 1-propanol compared to the polar aprotic VOC, acetone.[42] Ethanol generally has stronger binding affinities to the surface than a monopolar molecule such as acetone since the bipolar hydroxyl group in ethanol (OH) can possibly donate more charge to the surface than the carbonyl group in monopolar acetone molecules.[43]

We also compared the sensing performance of the heterojunction device with sensors consisting of only MoS_2 and only of Te shown in Figure 2e. Under the same test conditions (50 ppm ethanol under dark conditions), the response amplitude of the

ADVANCED
SCIENCE NEWS

www.advancedsciencenews.com
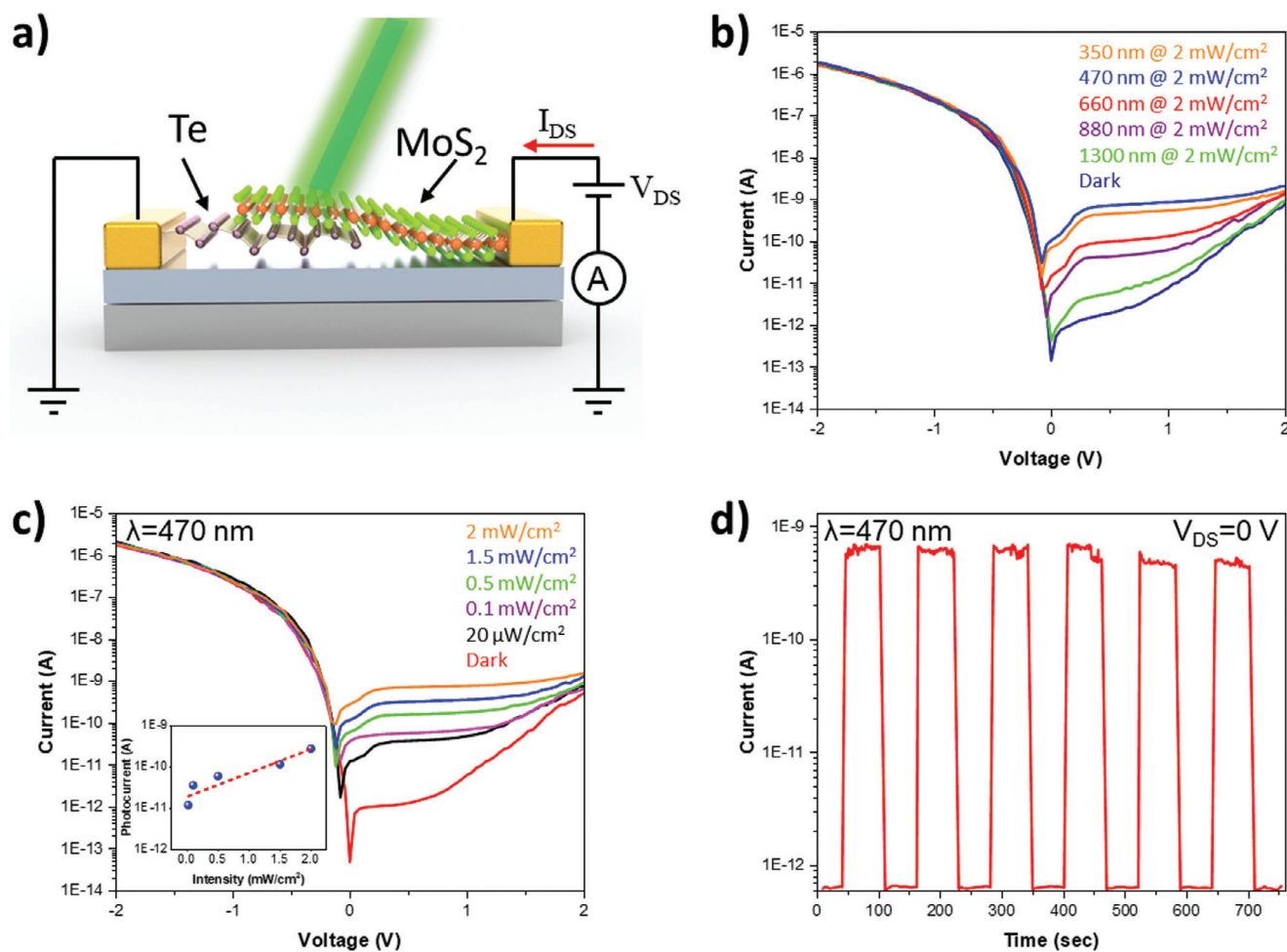
NANO · MICRO

small

www.small-journal.com
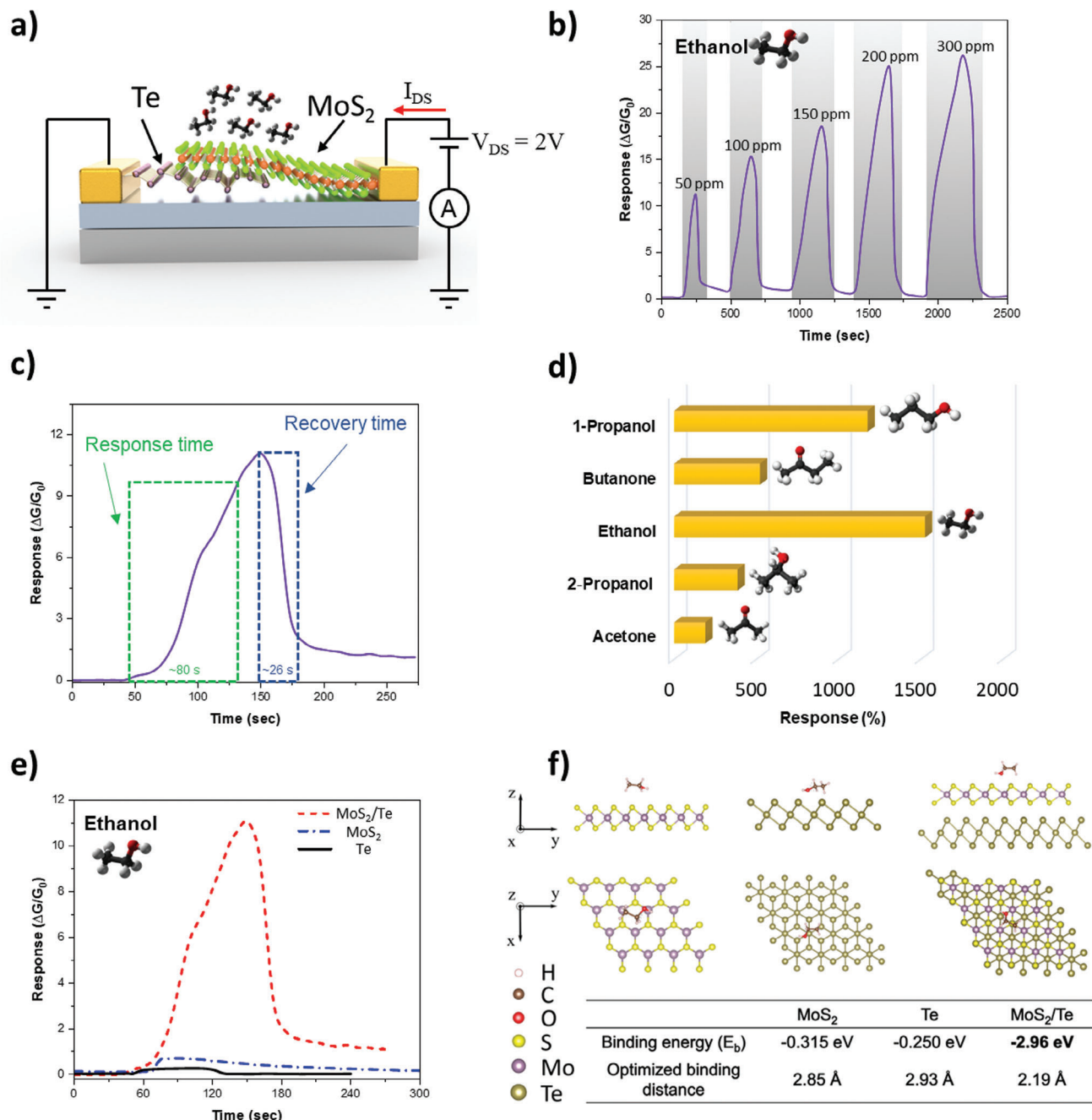
Figure 2. Heterojunction device response to VOCs while reverse biased at 2 V and under dark conditions. a) Schematic configuration of VOC sensing characterization; b) time-resolved response ($\Delta G/G_0$) of the device when exposed to ethanol at different concentrations in dark environment. The gray bars represent the combined response and recovery times of the device at each concentration; c) enlarged response toward 50 ppm of ethanol showing the response time (80 s) and recovery times (26 s); d) amplitude of the device response in dark environment to different VOCs each at 100 ppm; e) VOC sensing comparisons between individual MoS_2 (blue-dash dot), individual Te (black-solid), and MoS_2/Te heterojunction (red-dash) toward 50 ppm ethanol under dark conditions; f) Side and top views of the optimized structures of ethanol adsorbed on MoS_2 (left) tellurene (middle), and MoS_2/Te heterojunction (right), respectively. Magenta, yellow, golden, brown, red, and light pink balls represent Mo, S, Te, C, O, and H atoms, respectively.

heterojunction was >17× higher than that of the MoS_2 only sensor and >50× higher than of the Te only sensor. The enhanced VOC detection sensitivity agrees with the enhanced sensitivity reported in NO_2 and other gas sensors based on 2D-material heterojunctions.[22,27,44] The enhanced sensing performance of

van der Waals MoS_2/Te heterojunction to VOCs was further investigated by calculations of adsorption energies using DFT simulations as shown in Figure 2f. First, the MoS_2/Te heterojunction comprising of relatively large supercells of MoS_2 and tellurene was simulated. (Further details of the simulation parameters and

**ADVANCED
SCIENCE NEWS**

www.advancedsciencenews.com

NANO · MICRO

small

www.small-journal.com

Figure 3. The optoelectronic characteristics of the MoS₂/Te heterojunction. a) Schematic configuration for optical characterization; b) I-V curves of the device under illumination of different wavelengths (350–1300 nm); c) I-V curves of the heterojunction and corresponding photocurrents (inset) under different light intensities and d) photocurrent versus time under 2 mW-cm⁻² light intensity at a constant wavelength of $\lambda = 470$ nm.

optimized values are discussed in Figures S2–S4, Supporting Information). The lowest energy configuration was obtained by considering the different orientations of and varied binding distances of ethanol on MoS₂/Te heterojunction. The binding energy (E_b) was calculated by using the relation,

$$E_b = E_{ethanol@MoS2/Te} - E_{MoS2/Te} - E_{ethanol} \qquad (1)$$

where $E_{ethanol@MoS2/Te}$, $E_{MoS2/Te}$, and $E_{ethanol}$ represent the total energies of ethanol adsorbed on MoS₂/Te, bare MoS₂/Te, and isolated ethanol molecule, respectively. In the lowest energy configurations of ethanol adsorbed on MoS₂/Te heterojunction, a strong E_b value of −2.96 eV was obtained. The optimized binding distance of ethanol with MoS₂/Te heterojunction was found to be 2.19 Å. We then performed additional calculations to study the adsorption mechanism of ethanol on MoS₂, and Te monolayers separately and compare them with that of the heterojunction. The corresponding E_b values of ethanol were found as −0.315 eV on MoS₂, and −0.250 eV on tellurene with the optimized binding distance of 2.85 and 2.93 Å, respectively. It is evident from the E_b values that MoS₂/Te heterojunction adsorbed ethanol much

stronger than those of isolated MoS₂, and Te monolayers. Computational analysis of the adsorption of the representative VOC, ethanol, agrees with the experimental findings.

2.2. Optoelectronic Characteristics of the Heterojunction

The formation of a p-n heterojunction generates a built-in electric field, which facilitates operating the sensor in photovoltaic mode without an external bias (also referred to as self-powered mode). The optoelectronic characteristics of the heterojunction devices were investigated under incident light illuminated by light-emitting diodes (LEDs) of different wavelengths (λ = 350, 470, 660, 880, and 1300 nm) as depicted in schematic **Figure 3a**. The current–voltage (I-V) curves of the heterojunction in dark and under constant intensity of 2 mW-cm⁻² illumination at different wavelengths ranging from 350 to 1300 nm are illustrated in Figure 3b. Under dark conditions, the device showed a high diode rectification ratio, defined as |I(−1 V)/I(1 V)| of >10⁵ as a result of the p-n junction formed across the interface of n-type MoS₂ and p-type Te. Under light, the MoS₂/Te heterojunction

**ADVANCED
SCIENCE NEWS**

www.advancedsciencenews.com

NANO · MICRO

small

www.small-journal.com

device exhibited a broadband photoresponse. The photoresponsivity, $R = I_{ph}/P$, defined as the ratio of the photocurrent (I_{ph}) and the incident light power (P), had a maximum value of 4.7 A/W at $\lambda = 470$ nm under 2 mW·cm^{-2} light intensity.

The optoelectronic performance of the heterojunction was further characterized at a single wavelength of 470 nm with increasing power densities from dark condition to 2 mW cm^{-2} as shown in Figure 3c. The photocurrent rose exponentially with increasing light intensity as shown in the inset of Figure 3c due to the generation of the photogenerated electron-hole pairs (photoconductive generation mechanism).[45] The photocurrent increased from 4×10^{-14} A (dark) to 2×10^{-10} A at 0 V bias under 2 mW·cm^{-2} of 470 nm light. The time-dependent photocurrent (I-t) of the heterojunction device at $\lambda = 470$ nm under 2 mW·cm^{-2} light intensity at zero bias is plotted in Figure 3d. The MoS$_2$/Te device exhibited a stable and repeatable response with an I$_{(light)}$/I$_{(dark)}$ ratio of $\approx$1000.

2.3. Sensitivity Enhancement under Photovoltaic Zero-Bias Conditions

During operation in photovoltaic mode under illumination without external bias (self-powered mode), the sensitivity of the MoS$_2$/Te heterojunction for VOC detection can be enhanced further than under dark conditions. The photovoltaic VOC sensing characteristics of the heterojunction were investigated under light ($\lambda = 470$ nm at 20 mW·cm^{-2}) as illustrated in **Figure 4a**. Note that 470 nm corresponds to blue light, which could be harvested from sunlight or indoor lighting, or supplied by an LED light source.

Figure 4b illustrates the dynamic response of the sensor when exposed to 20–300 ppm concentration of butanone in photovoltaic mode without an external bias. The sensor response ($\Delta G/G_0$) to the lowest concentration of butanone (20 ppm) was as high as 40 which increased to 110 when the concentration was increased to 300 ppm. As the plotted responsivities for different concentrations of butanone shown in Figure 4c suggest, the photo-illumination-assisted sensing resulted in a significant enhancement in the device performance. For example, the response to 100 ppm of butanone increased from $\approx$500% under dark conditions with an applied reverse bias of 2 V (the exact value can be read from the bar chart in Figure 2d) to $\approx$7000% with illumination with zero bias. Therefore, photo-illumination-assisted VOC detection is a promising strategy to enhance VOC sensor sensitivity while potentially lowering power consumption. As shown in Figure 4d, the response and recovery time upon exposure to 20 ppm of butanone were measured to be 25 and 75 s, respectively, which is one of the shortest response times to butanone at room temperature reported for 2D material-based VOC sensors.[46] Although the primary mechanism influencing response and recovery times in gas sensors is still the adsorption and desorption of analyte molecules onto and from the sensor surface, illumination generally enhances the response and recovery times of heterostructure sensors by accelerating reaction kinetics, improving charge carrier dynamics, and facilitating gas adsorption/desorption processes. Different wavelengths and intensities of light can further optimize these effects, leading to improved sensor performance.[47]

Signal-to-noise-ratio (SNR) and the theoretical limit of detection (LOD) of the heterojunction were calculated to assess the signal quality and its immunity to the background noise in the photovoltaic mode of operation (Methodology is in Supporting Information). The SNR of the self-powered VOC sensing upon exposure to 300 ppm of butanone was calculated to be 2289.74, which is quite comparable with the reported heterojunction-based gas sensors.[27] The theoretical LOD for detection of butanone was also calculated to be 386 parts per billion (ppb) in photovoltaic zero-bias condition, which is comparable to the lowest concentration of butanone measured by biased sensors at room temperature reported in the literature.[46,48,49]

2.4. Environmental Effects and Stability Test

The effect of illumination power on the self-powered VOC sensing performance was also investigated. The transient response of the heterojunction toward 150 ppm of ethanol and 1-propanol under 470 nm light with three different intensities are illustrated in Figure S5 (Supporting Information). The response toward ethanol and 1-propanol monotonically increased from $\approx$3 to $\approx$8 and from $\approx$4 to $\approx$19, respectively, when the illumination intensity increased from 0.5 to 20 mW·cm^{-2}. At greater light intensities, the stronger built-in electric field can efficiently separate the photogenerated electron-hole pairs, reducing recombination rates and increasing charge carrier lifetimes. The facilitated charge separation along with more charge carriers enhances sensitivity to VOC-surface interactions, ultimately leading to the observed enhancement of sensing performance.[44] It should be noted that the observed trend is not monotonic, that is, the maximum sensitivity is associated with an optimum light intensity value beyond which the responsivity starts declining, which may be due to the desorption rate surpassing the adsorption rate at very high intensities.[50]

Moreover, the effect of environmental conditions on the sensor time-resolved response was investigated. Figure S6a (Supporting Information) shows the device average response when exposed to 100 ppm ethanol in photovoltaic mode without an external bias under 470 nm illumination at an intensity of 20 mW·cm^{-2}. Throughout a 35-day exposure to the air, the average response declined by $\approx$14% from its initial value, suggesting good long-term stability in air. The effect of relative humidity, another important environmental factor on sensor response, is shown in Figure S6b (Supporting Information). The sensor response to 50 ppm of Butanone under 470 nm light at an intensity of 20 mW·cm^{-2} and 0 V bias monotonically decreased as the relative humidity (RH) increased from 35% to 90% at room temperature. The water molecules occupy the available active sites on the heterojunction and act like a barrier between the VOC molecules and the surface, lowering responsivity of the heterojunction device toward the target VOC. The observed effect agrees with the results previously reported for 2D material-based gas sensors.[38]

2.5. VOC Sensing Mechanism

The mechanism of the self-powered VOC sensor can be explained using the band diagrams of MoS$_2$/Te heterojunction
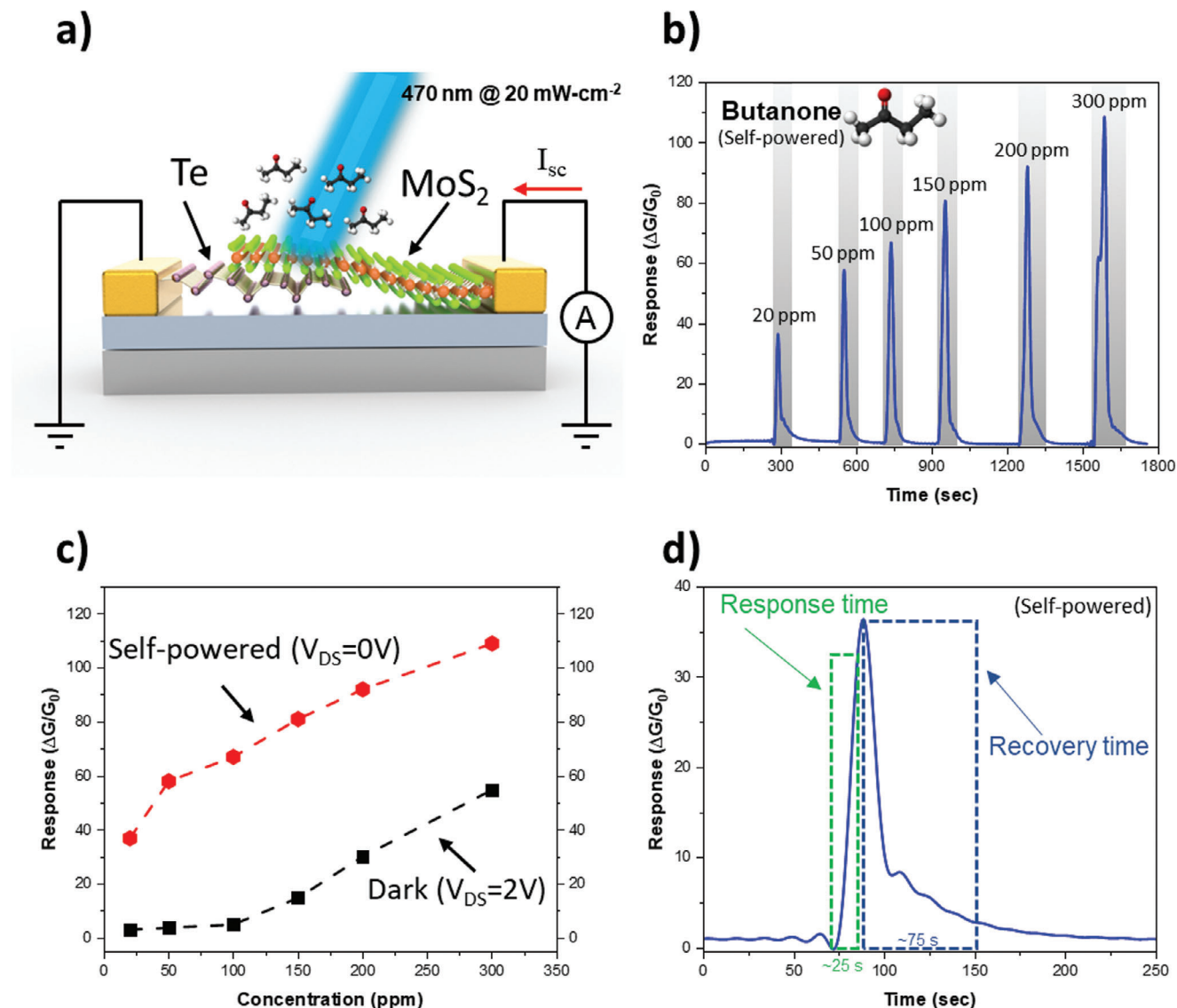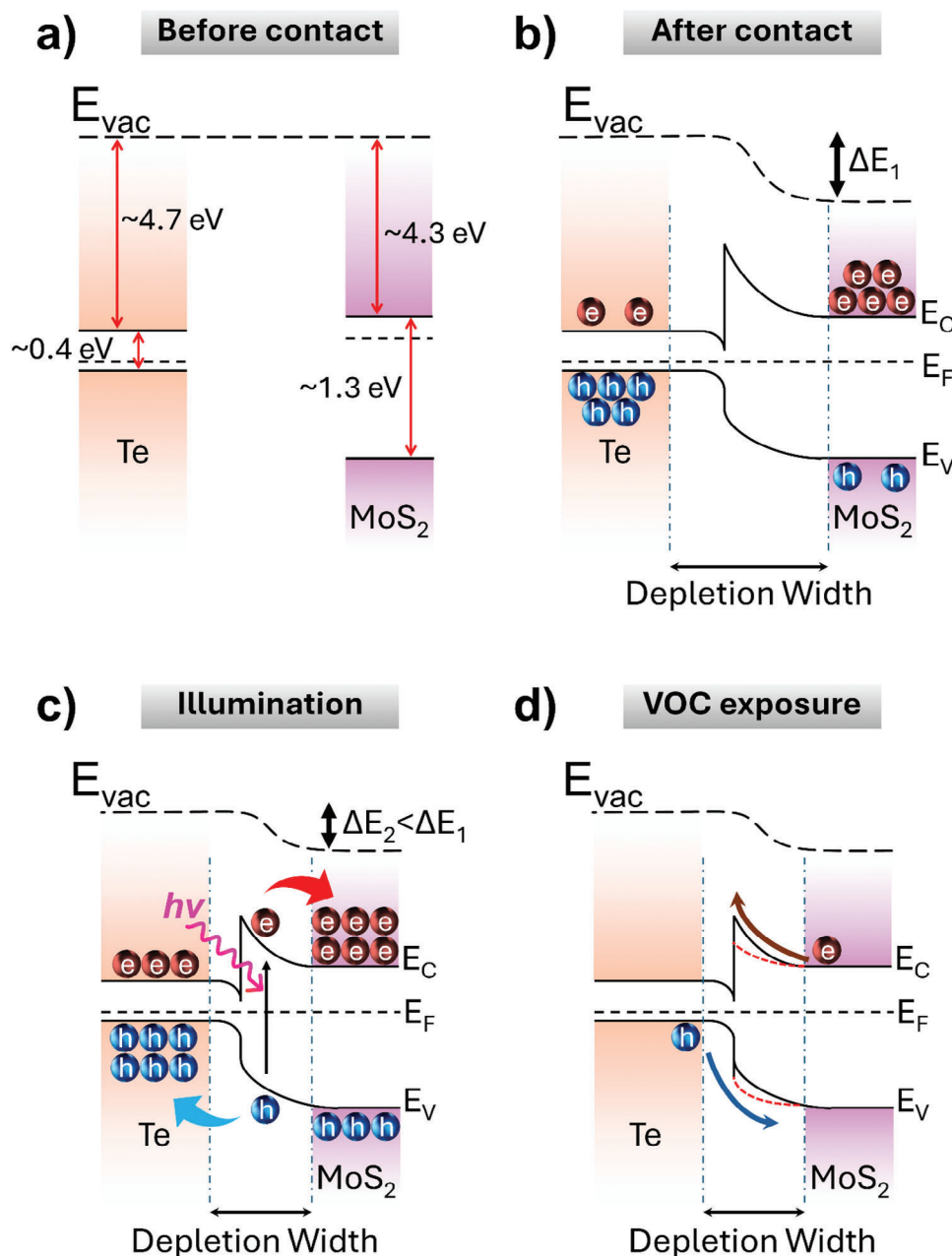
Figure 4. Photovoltaic zero-bias (self-powered) VOC sensing of the device under illumination of $\lambda = 470$ nm. a) Schematic illustration of photovoltaic VOC sensor measurement setup; b) time-resolved response of the device toward different concentrations of butanone. The gray bars represent the combined response and recovery times of the device at each concentration; c) the device response comparison between dark conditions with an applied reverse bias of 2 V and photovoltaic mode at zero bias voltage when exposed to butanone at different concentrations from 20 to 300 ppm; d) the response time (25 s) and recovery times (75 s) of the device toward 20 ppm of butanone.

schematically illustrated in **Figure 5**. The isolated multilayer Te and MoS_2 are semiconductors with bandgap energies of ≈ 0.40 and ≈ 1.3 eV, and electron affinities of ≈ 4.7 and ≈ 4.3 eV, respectively (Figure 5a).[38,51,52] When the two materials are brought into physical contact (Figure 5b), both the conduction and the valence bands bend at the interface due to the difference in the position of their Fermi levels. A downward band bending near the Te surface and an upward band bending near the MoS_2 surface align the Fermi levels of the MoS_2/Te p-n junction, achieving equilibrium as illustrated in Figure 5b. A built-in electric field is then created in the junction, and a type-I (straddling gap) heterostructure is formed in the equilibrium state since the conduction band (CB) of MoS_2 is higher, and the valence band (VB) is lower than the

corresponding bands of Te as illustrated in the band alignment in Figure 5a.

Upon illumination as shown in Figure 5c, the photogenerated electron-hole pairs are separated by the built-in electric field of the p-n junction; as a result, the photogenerated electrons migrate to n-type MoS_2 and the photogenerated holes to p-type Te, generating short-circuit current, I_{sc}, at zero bias voltage. This process increases the potential of the n-type region and decreases the potential of the p-type region, creating an opposing voltage to the internal built-in electric field, equivalent to a forward bias. This results in a decrease in the depletion region width, potential barrier, and p-n junction resistance, and increase in diffusion current.[53]

**ADVANCED
SCIENCE NEWS**

www.advancedsciencenews.com

**NANO · MICRO
small**

www.small-journal.com

Figure 5. The energy band diagram and VOC sensing mechanism. a) energy band diagram of MoS_2 and Te before forming the junction; b) energy band diagram of MoS_2/Te heterojunction; c) separation of photogenerated charge carriers; d) charge transfer between VOC molecules and the heterojunction.

Adsorption of VOC molecules increases the carrier concentration in the junction (Figure 5d) since the adsorbed VOC molecules contribute extra charge carriers and hence increase the conductance (G) of device.[27,44] Therefore, the initial conductance of the sensor (G_0) undergoes a change (ΔG) when the VOC molecules are introduced and recovers to near its initial conductance as the VOC molecules desorb from the heterojunction surface. The high sensitivity of heterojunctions is associated with band alignment modulation at the interface.[54] The electron density at the junction interface increases as VOC molecules donate electrons, shifting the Fermi level of MoS_2 upward and reducing

the barrier height at the MoS_2/Te interface. The current across the heterojunction can be described by the following equation based on thermionic emission model[53]

$$I = AA^*T^2\exp\left(-\frac{e\varphi}{kT}\right)\left[\exp\left(\frac{eV}{nkT}\right) - 1\right] \tag{2}$$

where I, e, V, n, k, T, A, A^*, and φ denote heterojunction current, electron charge, applied voltage, diode ideality factor, Boltzmann constant, absolute temperature, effective junction area, Richardson's constant, and junction barrier height, respectively.

ADVANCED
SCIENCE NEWS

www.advancedsciencenews.com

NANO · MICRO

small

www.small-journal.com

Using Equation (2), the change in the barrier height upon exposure to VOC molecules can be determined by comparing the heterojunction current before VOC exposure, $I_{without\_VOC}$, and after VOC exposure, I_{VOC}:

$$e\Delta\varphi = -kT\ln\left(\frac{I_{VOC}}{I_{without\_VOC}}\right) \qquad (3)$$

From Equation (3), we can calculate the changes in junction barrier height with varying butanone concentrations from 20 to 300 ppm, as represented in Table S1 (Supporting Information). The lowered barrier height due to butanone adsorption, as indicated by the dotted red line in Figure 5d, increases electrical current across the junction by allowing more photogenerated carriers to overcome the barrier at the MoS_2/Te interface.

Due to the exponential dependence of heterojunction current on the barrier height, even a minor change in barrier height significantly affects the current, leading to a highly sensitive response to VOC molecules compared to individual MoS_2 and Te VOC sensors. Feng et al. simulated the band diagram of a BP/$MoSe_2$ heterojunction with bandgap energies of 0.35 and 1.2 eV, respectively.[54] This heterojunction exhibited a band alignment similar to that of the MoS_2/Te heterojunction. The calculations of BP/$MoSe_2$ band bending revealed that a 10% decrease in carrier concentration due to NO_2 adsorption (where NO_2 captures electrons from the heterojunction, unlike VOCs) can increase the barrier height from 0.26 to 0.34 eV, resulting in a sharp current drop of an approximate factor of two. In contrast, a $MoSe_2$ only device, experiencing the same decline in carrier concentration upon NO_2 adsorption, would have exhibited only a ≈10% current drop. Their findings align with the observed significant improvement in the MoS_2/Te heterojunction response shown in Figure 2e compared to the MoS_2 only sensor and the Te only sensor responses.

To further assess the VOC sensing performance of MoS_2/Te heterojunction and to compare it with that of the 2D-material-based heterostructures reported in the literature, their key performance indicators including operating temperature, responsivity, and response/recovery time are listed in Table 1.

3. Conclusion

In summary, the photovoltaic MoS_2/Te heterojunction-based VOC sensors were fabricated by transferring mechanically-exfoliated MoS_2 crystals onto 2D hydrothermally synthesized Te flakes. The VOC detection sensitivity was enhanced by the MoS_2/Te heterojunction under dark conditions as compared to the individual MoS_2 and Te VOC sensors. The sensitivity was further enhanced by photoillumination at zero bias voltage demonstrating VOC detection with superior response, and relatively short response and recovery times. In particular, the response of the device toward butanone was ≈7000% at room temperature. The self-powered sensing is attributed to the built-in electric field at the junction and its ability to effectively separate photogenerated carriers. The VOC sensing performance of the MoS_2/Te heterojunction shown by experimental measurements and DFT simulations suggests that it holds potential as low-power-consumption sensing platform for wearable or portable applications including hazardous environmental monitoring, non-invasive diagnostic screening, and process control.

4. Experimental Section

Synthesis of Te Nanoflakes: A hydrothermal process was employed to synthesize 2D Te nanoflakes using TeO_2, NaOH, and glucose as the process precursors. At room temperature, 0.4 g of NaOH, 0.2 g of glucose, and 0.4 g of TeO_2 were dissolved in 80 mL of deionized (DI) water. A uniform solution was then obtained through 20 min sonication of the mixture. Subsequently, the solution was transferred to a Teflon-lined autoclave with a capacity of 100 mL and heated for 1 h at 180 °C to synthesize 2D Te nanoflakes. Te nuclei gradually form in a pressurized autoclave reactor as TeO_3 anions were reduced by C_2H_6O. Glucose acts as a surfactant agent to limit the anisotropic growth of Te crystals in [001] direction.[65,66] Finally, the as-synthesized Te crystals were collected by centrifugation and underwent three rounds of washing with ethanol and 2-propanol to eliminate any chemical residues.

Fabrication of MoS2/Te Heterojunction: A p-type (100) Si wafer of resistivity ≤0.005 Ω-cm with 300 nm thermally oxidized SiO_2 was cleaned in acetone, 2-propanol, and DI water ultrasonication baths for 10 min each. The Te precursor solution was then drop-casted on SiO_2/Si substrates and baked at 100 °C. The drop-casted flakes were inspected under an optical microscope to identify a trapezoid-shape flake with proper thicknesses. To fabricate the electrode contacting Te flake, the SiO_2/Si substrate with Te nanoflakes was coated with Microposit S1813 photoresist and underwent through a photolithography process, thermal evaporation, and lift-off in an acetone bath to deposit the electrode with thicknesses of 10 nm Cr and 60 nm Au on the Te flake. MoS_2 flakes were mechanically exfoliated from a bulk MoS_2 crystal (SPI supplies) using Nitto SPV224 tape and transferred onto a new SiO_2/Si substrate. After inspection and selecting the desired flake, a standard PMMA-assisted method was employed to transfer the MoS_2 flake onto the target substrate where the thin PMMA film attached to the MoS_2 nanoflake was aligned under an optical microscope so that the transferred MoS_2 precisely overlapped with the Te nanoflake. Finally, the PMMA was removed in acetone bath, and the second 10/60 nm Cr/Au electrode was patterned and deposited in the same fashion as the first one.

Device Characterization: The thickness of the nanoflakes was measured in an atomic force microscopy MFP-3D AFM (Asylum Research, Santa Barbara). Raman spectroscopy (Renishaw, 514 nm excitation laser) was employed to verify the MoS_2 and Te crystals using a Renishaw inVia confocal Raman microscope under a 514 nm continuous-wave excitation laser. XPS characterization was done employing a monochromatic aluminum source (Al K, 1486.6 eV) running at 150 W in a Kratos Analytical Axis ULTRA spectrometer with a DLD spectrometer. The electrical and photovoltaic characterizations of the heterojunction device were carried out using a semiconductor characterization system connected to a probe station (Keithley 4200-SCS) along with a spectrometer (Thorlabs, PM100D, USA) and different wavelength LEDs.

VOC Sensing Measurement: All the VOC sensing tests were performed in a home-built gas sensing setup. The heterojunction device was fixed inside an enclosed chamber stage (Linkam,

Table 1. A comparison of the VOC sensing performances of 2D-material heterojunctions.

	Target VOCs	Operating Temperature [°C]	Sensing Sensitivity [%] (VOC and concentration)	Response/Recovery time [s]	Self-Powered	Reference
MoS_2/Graphene	Toluene	RT	12.5 (Toluene, 10% Saturated Vapor)	NA	N	[55]
rGO/Co_3O_4	Ethanol, Acetone, Methanol, Toluene, Xylene, and n-butyl alcohol	200 °C	2100 (Ethanol, 100 ppm)	≈30/≈60	N	[56]
MXene/SnO_2	Ethanol, Methanol, Acetone, and Formaldehyde	RT	3.12 (Ethanol, concentration not reported)	NA	N	[57]
SnS_2/SnS	Ethanol	RT	11 (Ethanol, 4 ppm)	≈500/≈1200	N	[58]
MoS_2/TiO_2	Ethanol and Methanol	150 °C	1420 (Ethanol, 100 ppm)	≈15/≈15	N	[59]
GO/ZnO	Ethanol, Acetone, and Ethylbenzene	RT	32 (Ethanol, 1 ppm)	≈190/≈200	N	[60]
rGO/SnO_2	Phenol, Methanol, Benzene, Methylbenzene, and Ethanol	RT	1.6 (Phenol, 60 ppb)	2.4/1.06	N	[61]
$Ti_3C_2T_x$/WSe_2	Ethanol, Methanol, Acetone, Hexane, Benzene, and Toluene	RT	9.2 (Ethanol, 40 ppm)	9.7/6.6	N	[62]
La@MoS_2	Acetone, Chloroform, Ethanol, Isopropanol, and Methanol	RT	20.1 (Acetone, 500 ppm)	48.5/43.2	N	[63]
WS_2/ZnS	Ethanol, Methanol, Toluene, and Acetone	RT	63 (Toluene, 1% Saturated Vapor)	NA	N	[64]
MoS_2/GaSe	Methanol, Ethanol, and Acetone	RT	≈5 (Ethanol, 500 ppm)	NA	Y	[27]
MoS_2/Te	Acetone, 2-propanol, 1-propanol, Butanone, and ethanol	RT	≈7000 (Butanone, 100 ppm)	25/75	Y	This work

HFS350EV-PB4) using tungsten probes that were connected to the outlet of a gas sampling bulb. A flow controller regulated the flow of N_2, used as the carrier gas, to the inlet of the gas sampling bulb. The desired VOC concentrations, C_{ppm}, were calculated using the following formula, and the corresponding volume of liquid VOC was injected into the gas sampling bulb using a syringe.[38]

$$C_{ppm} = \frac{T(K) \times \rho \times R \times V_{Liquid}}{p \times M_{Liquid} \times V_{chamber}} \quad (4)$$

p (kPa) and T (K) denotes the pressure and temperature inside the chamber, ρ (g.mL^{-1}) is the density of VOCs, R is the gas con-

stant, M (kg.mol^{-1}) is the molecular weight of liquid VOC, and V_{Liquid} and $V_{chamber}$ are the volume of injected liquid VOC and the volume of the chamber, respectively.

All the sensing measurements were performed at room temperature (25 °C). Before any VOC measurements, the devices were exposed to approximately a 10-min flow of N_2 for stabilization. LED lights of different wavelength were mounted on the top window of the gas-sensing chamber and directly illuminated the sensor. In self-powered mode, no external bias voltage was applied to the sensors while the device was illuminated with 470 nm LED light source. The real-time current signal was measured using a Keithley 2400 source meter. The sensor response was defined as $\Delta G/G_0$, which ΔG and G_0 denote the change in

conductance due to VOC and the initial conductance before exposure to VOC, respectively.

5. Computational Methods

In order to study the atomic-scale sensing mechanism of VOCs on MoS_2/Te heterojunction, first principles DFT calculations were performed with projected augmented wave method and the generalized gradient approximation (GGA).[67,68] Spin-polarized GGA within Perdew–Burke–Ernzerhof (PAW-PBE) were employed for the exchange-correlation functionals, as implemented in VASP code.[67,69,70] Well known underestimation of the binding mechanism caused by GGA-PBE was corrected through the inclusion of van der Waals interactions at DFT-D3 method as proposed by Grimme.[71] While studying the sensing of VOCs, specifically ethanol, on tellurene (Te), and MoS_2/Te heterojunction, vacuum space of 30 Å was inserted along the vertical direction to avoid unwanted interactions between the periodic images. The sampling of Brillouin zone was executed under Monkhorst-Pack scheme with the KPOINTS mesh of $5 \times 5 \times 1$.[72] Energy cut-off value of 550 eV was used through the calculations for the plane wave basis set. Ground state geometries were obtained by relaxing the atomic positions and keeping the cell volume fixed. We used a convergence criterion between two ionic steps as 10^{-6} eV, whereas the forces were converged at 0.01 eV Å^{-1}.

Supporting Information

Supporting Information is available from the Wiley Online Library or from the author.

Conflict of Interest

The authors declare no conflict of interest.

Author Contributions

M.R.M. and A.H. contributed equally to this work. M.R.M. and A.H. conceptualized the project and performed all experimental measurements under the supervision of M.M.A. and R.K.N.D.R. M.R.M. fabricated the sensors and prepared the manuscript. A.H., A.A., and M.M.A. revised the manuscript. F.K. participated in device fabrication. T.H. performed all DFT simulations and analysis. H.G., M.F., A.A., R.A., F.K., and T.D.S. contributed to data validation. The manuscript was written through contributions of all authors. All authors have given approval to the final version of the manuscript.

[1] A. K. Pathak, C. Viphavakit, *Sens. Actuators, A* **2022**, *338*, 113455.
[2] M. Khatib, H. Haick, *ACS Nano* **2022**, *516*, 7080.
[3] J. Zhu, Z. Ren, C. Lee, *ACS Nano* **2020**, *15*, 894.
[4] A. H. Jalal, F. Alam, S. Roychoudhury, Y. Umasankar, N. Pala, S. Bhansali, *ACS Sens.* **2018**, *3*, 1246.
[5] P. Velusamy, C. H. Su, P. Ramasamy, V. Arun, N. Rajnish, P. Raman, V. Baskaralingam, S. M. S. Kumar, S. C. Gopinath, *Crit. Rev. Anal. Chem.* **2023**, *53*, 1828.
[6] Y. Saalberg, M. Wolff, *Clin. Chim. Acta* **2016**, *459*, 5.
[7] V. Saasa, T. Malwela, M. Beukes, M. Mokgotho, C. P. Liu, B. Mwakikunga, *Diagnostics* **2018**, *8*, 12.
[8] M. Shirasu, K. Touhara, *J. Biochem.* **2011**, *150*, 257.
[9] W. C. Tan, K. W. Ang, *Adv. Electron. Mater.* **2021**, *7*, 2001071.
[10] R. Kumar, X. Liu, J. Zhang, M. Kumar, *Nano-Micro Lett.* **2020**, *12*, 164.
[11] J. An, X. Zhao, Y. Zhang, M. Liu, J. Yuan, X. Sun, Z. Zhang, B. Wang, S. Li, D. Li, *Adv. Funct. Mater.* **2022**, *32*, 2110119.
[12] T. Li, T. Jing, D. Rao, S. Mourdikoudis, Y. Zuo, M. Wang, *Inorg. Chem. Front.* **2022**, *9*, 6008.
[13] H. L. Hou, C. Anichini, P. Samorì, A. Criado, M. Prato, *Adv. Funct. Mater.* **2022**, *32*, 2207065.
[14] Z. Li, Z. Yao, A. A. Haidry, Y. Luan, Y. Chen, B. Y. Zhang, K. Xu, R. Deng, N. D. Hoa, J. Zhou, J. Z. Ou, *Nano Today* **2021**, *40*, 101287.
[15] D. J. Buckley, N. C. Black, E. G. Castanon, C. Melios, M. Hardman, O. Kazakova, *2D Mater.* **2020**, *7*, 032002.
[16] A. Chaves, J. G. Azadani, H. Alsalman, D. R. Da Costa, R. Frisenda, A. J. Chaves, S. H. Song, Y. D. Kim, D. He, J. Zhou, A. Castellanos-Gomez, *npj 2D Mater. Appl.* **2020**, *4*, 29.
[17] W. Zheng, X. Liu, J. Xie, G. Lu, J. Zhang, *Coord. Chem. Rev.* **2021**, *447*, 214151.
[18] R. Kumar, W. Zheng, X. Liu, J. Zhang, M. Kumar, *Adv. Mater. Technol.* **2020**, *5*, 1901062.
[19] Z. Shi, R. Cao, K. Khan, A. K. Tareen, X. Liu, W. Liang, Y. Zhang, C. Ma, Z. Guo, X. Luo, H. Zhang, *Nano-Micro Lett.* **2020**, *12*, 99.
[20] T. Zhu, Y. Zhang, X. Wei, M. Jiang, H. Xu, *Front. Phys.* **2023**, *18*, 33601.
[21] S. Dhara, H. Jawa, S. Ghosh, A. Varghese, D. Karmakar, S. Lodha, *ACS Appl. Mater. Interfaces* **2021**, *13*, 30785.
[22] Z. Feng, B. Chen, S. Qian, L. Xu, L. Feng, Y. Yu, R. Zhang, J. Chen, Q. Li, Q. Li, C. Sun, *2D Mater.* **2016**, *3*, 035021.
[23] H. Tabata, H. Matsuyama, T. Goto, O. Kubo, M. Katayama, *ACS Nano* **2021**, *15*, 2542.
[24] L. Liu, M. Ikram, L. Ma, X. Zhang, H. Lv, M. Ullah, M. Khan, H. Yu, K. Shi, *J. Hazard. Mater.* **2020**, *393*, 122325.
[25] M. Ikram, L. Liu, Y. Liu, L. Ma, H. Lv, M. Ullah, L. He, H. Wu, R. Wang, K. Shi, *J. Mater. Chem. A* **2019**, *7*, 14602.
[26] J. Yao, G. Yang, *Adv. Sci.* **2022**, *9*, 2103036.
[27] Y. Niu, J. Zeng, X. Liu, J. Li, Q. Wang, H. Li, N. F. Rooij, Y. Wang, G. Zhou, *Adv. Sci.* **2021**, *8*, 2100472.

[28] J. Zhang, L. Liu, Y. Yang, Q. Huang, D. Li, D. Zeng, *Phys. Chem. Chem. Phys.* **2021**, *23*, 15420.

[29] F. de Souza, R. K. Gupta, *2D Nanomaterials*, CRC Press, Boca Raton, FL **2022**, pp. 53–70.

[30] J. M. Song, Y. Z. Lin, Y. J. Zhan, Y. C. Tian, G. Liu, S. H. Yu, *Crystal Growth Design* **2008**, *8*, 1902.

[31] Y. Wang, G. Qiu, R. Wang, S. Huang, Q. Wang, Y. Liu, Y. Du, W. A. Goddard III, K. MJ, X. Xu, Y. PD, *Nat. Electron.* **2018**, *1*, 228.

[32] A. Abnavi, R. Ahmadi, H. Ghanbari, M. Fawzy, A. Hasani, T. De Silva, A. M. Askar, M. R. Mohammadzadeh, F. Kabir, M. Whitwick, M. Beaudoin, *Adv. Funct. Mater.* **2023**, *33*, 2210619.

[33] Y. R. Kumar, K. Deshmukh, T. Kovářík, S. K. Pasha, *Coord. Chem. Rev.* **2022**, *461*, 214502.

[34] S. Öztürk, A. Kösemen, Z. A. Kösemen, N. Kılınç, Z. Z. Öztürk, M. Penza, *Sens. Actuators, B* **2016**, *222*, 280.

[35] A. Singh, S. Sikarwar, A. Verma, B. C. Yadav, *Sens. Actuators, A* **2021**, *332*, 113127.

[36] B. Zong, Q. Xu, Q. Li, X. Fang, X. Chen, C. Liu, J. Zang, Z. Bo, S. Mao, *J. Mater. Chem. A* **2021**, *9*, 14411.

[37] S. Acharyya, S. Nag, S. Kimbahune, A. Ghose, A. Pal, P. K. Guha, *ACS Sens.* **2021**, *6*, 2218.

[38] M. R. Mohammadzadeh, A. Hasani, K. Jaferzadeh, M. Fawzy, T. De Silva, A. Abnavi, R. Ahmadi, H. Ghanbari, A. Askar, F. Kabir, R. K. Rajapakse, *Adv. Sci.* **2023**, *10*, 2205458.

[39] W. M. Zhang, J. S. Hu, W. G. Song, L. J. Wan, *Sens. Actuators, B* **2007**, *123*, 454.

[40] M. Lapuerta, J. P. Hernández, J. R. Agudelo, *Appl. Therm. Eng.* **2014**, *73*, 539.

[41] Y. Farajollahi, Z. Chen, F. Haghighat, *CLEAN–Soil, Air, Water* **2009**, *37*, 436.

[42] T. T. Tung, M. T. Tran, J. F. Feller, M. Castro, T. Van Ngo, K. Hassan, M. J. Nine, D. Losic, *Carbon* **2020**, *159*, 333.

[43] A. A. Abokifa, K. Haddad, J. Fortner, C. S. Lo, P. Biswas, *J. Mater. Chem. A* **2018**, *6*, 2053.

[44] M. Mathew, P. V. Shinde, R. Samal, C. S. Rout, *J. Mater. Sci.* **2021**, *56*, 9575.

[45] H. Ghanbari, A. Abnavi, A. Hasani, F. Kabir, R. Ahmadi, M. R. Mohammadzadeh, M. Fawzy, T. De Silva, M. M. Adachi, *Nanotechnology* **2023**, *34*, 285207.

[46] A. K. Singh, N. K. Chowdhury, A. Hazra, B. Bhowmik, *J. Electron. Mater.* **2023**, *52*, 3622.

[47] S. Ganesh Moorthy, M. Bouvet, *Sensors* **2024**, *24*, 1571.

[48] T. N. Oliveira, C. A. Zito, T. M. Perfecto, G. M. Azevedo, D. P. Volanti, *New J. Chem.* **2020**, *44*, 15574.

[49] H. Zhu, Z. Yuan, Y. Shen, H. Gao, F. Meng, *ACS Sens.* **2023**, *8*, 2635.

[50] Z. Feng, Y. Xie, E. Wu, Y. Yu, S. Zheng, R. Zhang, X. Chen, C. Sun, H. Zhang, W. Pang, J. Liu, *Micromachines.* **2017**, *8*, 155.

[51] A. Abnavi, R. Ahmadi, A. Hasani, M. Fawzy, M. R. Mohammadzadeh, T. De Silva, N. Yu, M. M. Adachi, *ACS Appl. Mater. Interfaces* **2021**, *13*, 45843.

[52] J. Yao, F. Chen, J. Li, J. Du, D. Wu, Y. Tian, C. Zhang, J. Yang, X. Li, P. Lin, *J. Mater. Chem. C* **2021**, *9*, 13123.

[53] W. Zheng, Y. Xu, L. Zheng, C. Yang, N. Pinna, X. Liu, J. Zhang, *Adv. Funct. Mater.* **2020**, *30*, 2000435.

[54] Z. Feng, B. Chen, S. Qian, L. Xu, L. Feng, Y. Yu, R. Zhang, J. Chen, Q. Li, Q. Li, C. Sun, *2D Materials* **2016**, *3*, 035021.

[55] T. Pham, P. Ramnani, C. C. Villarreal, J. Lopez, P. Das, I. Lee, M. R. Neupane, Y. Rheem, A. Mulchandani, *Carbon* **2019**, *142*, 504.

[56] M. Tian, J. Miao, P. Cheng, H. Mu, J. Tu, J. Sun, *Appl. Surf. Sci.* **2019**, *479*, 601.

[57] T. He, W. Liu, T. Lv, M. Ma, Z. Liu, A. Vasiliev, X. Li, *Sens. Actuators, B* **2021**, *329*, 129275.

[58] Q. Sun, J. Wang, J. Hao, S. Zheng, P. Wan, T. Wang, H. Fang, Y. Wang, *Nanoscale* **2019**, *11*, 13741.

[59] P. X. Zhao, Y. Tang, J. Mao, Y. X. Chen, H. Song, J. W. Wang, Y. Song, Y. Q. Liang, X. M. Zhang, *J. Alloys Compd.* **2016**, *674*, 252.

[60] E. Pargoletti, U. H. Hossain, I. Di Bernardo, H. Chen, T. Tran-Phu, J. Lipton-Duffin, G. Cappelletti, A. Tricoli, *Nanoscale* **2019**, *11*, 22932.

[61] D. Guo, P. Cai, J. Sun, W. He, X. Wu, T. Zhang, X. Wang, X. Zhang, *Carbon* **2016**, *99*, 571.

[62] W. Y. Chen, X. Jiang, S. N. Lai, D. Peroulis, L. Stanciu, *Nat. Commun.* **2020**, *11*, 1302.

[63] K. Rathi, A. N. Kumar, K. Pal, *Nanotechnology* **2020**, *31*, 395504.

[64] Y. Han, Y. Liu, C. Su, S. Wang, H. Li, M. Zeng, N. Hu, Y. Su, Z. Zhou, H. Wei, Z. Yang, *Sens. Actuators, B* **2019**, *296*, 126666.

[65] A. Hasani, M. R. Mohammadzadeh, H. Ghanbari, M. Fawzy, T. D. Silva, A. Abnavi, R. Ahmadi, A. M. Askar, F. Kabir, R. K. Rajapakse, M. M. Adachi, *ACS Omega* **2022**, *7*, 48383.

[66] P. Yu, L. Zhou, Z. Jia, K. Wu, J. Cui, *J. Mater. Sci., Mater. Electron.* **2020**, *31*, 16332.

[67] G. Kresse, D. Joubert, *Phys. Rev. B* **1999**, *59*, 1758.

[68] P. E. Blöchl, *Phys. Rev. B* **1994**, *50*, 17953.

[69] G. Kresse, J. Furthmüller, *Comput. Mater. Sci.* **1996**, *6*, 15.

[70] G. Kresse, J. Furthmüller, *Phys. Rev. B* **1996**, *54*, 11169.

[71] S. Grimme, *J. Comput. Chem.* **2006**, *27*, 1787.

[72] H. J. Monkhorst, J. D. Pack, *Phys. Rev. B* **1976**, *13*, 5188.